Dynamics of electric-field domains and oscillations of the photocurrent in a simple superlattice model

L. L. Bonilla, J. Galán,* J. A. Cuesta, F. C. Martínez, and J. M. Molera

Escuela Politécnica Superior, Universidad Carlos III de Madrid, Butarque 15, 28911 Leganés, Spain

(Received 22 April 1994)

A discrete model is introduced to account for the time-periodic oscillations of the photocurrent in a superlattice observed by Kwok *et al.* in an undoped 40-period AlAs/GaAs superlattice. The basic ingredients are an effective negative-differential resistance due to the sequential resonant tunneling of the photoexcited carriers through the potential barriers, and a rate equation for the holes that incorporates photogeneration and recombination. The photoexciting laser acts as a damping factor ending the oscillations when its power is large enough. The model explains (i) the known oscillatory static *I-V* characteristic curve through the formation of a domain wall connecting high- and low-electric-field domains, and (ii) the photocurrent and photoluminescence time-dependent oscillations after the domain wall is formed. In our model, they arise from the combined motion of the wall and the shift of the values of the electric field at the domains. Up to a certain value of the photoexcitation, the nonuniform field profile with two domains turns out to be metastable: after the photocurrent oscillations have ceased, the field profile slowly relaxes toward the uniform stationary solution (which is reached on a much longer time scale). Multiple stability of stationary states and hysteresis are also found. An interpretation of the oscillations in the photoluminescence spectrum is also given.

I. INTRODUCTION

In recent experiments by Kwok *et al.* the time-dependent transport properties of photoexcited undoped superlattices were investigated.[1] In a typical example, an undoped 40-period AlAs/GaAs superlattice was mounted in a *p-i-n* diode and continuously illuminated by laser light at 4 K. When the laser power was in a certain interval and the applied dc voltage bias was large enough, damped time-dependent oscillations of the photocurrent (PC) and the peaks in the photoluminescence (PL) spectrum were observed. The applied fields in the experiment[1] are high, the potential barriers are wide (between 30 and 40 Å), and the minibands correspondingly narrow, so that the coherence length is comparable to or smaller than the width of one quantum well. Then the quantum wells in the superlattice are weakly coupled and formation of electric-field domains may appear.[2-6] The subject of formation and expansion of electric-field domains in (doped) superlattices is an old one and it goes back to the conductance measurements of Esaki and Chang in 1974.[7] Typically, the dominant transport process in each domain is resonant tunneling between different subbands of the wells belonging to the domain.

Time-dependent oscillations of the PC in undoped illuminated superlattices have also been observed by Le Person *et al.*[8] for quite different superlattices where miniband transport is prevalent (narrow barriers, so that the quantum wells are not weakly coupled; in these conditions it is not clear whether formation and propagation of electric-field domains are relevant). These measurements were interpreted in terms of Gunn dipole domains of a classical drift-diffusion model.

In experiments with weakly coupled superlattices at high electric fields, the dominant transport mechanism is resonant tunneling: It follows from Kazarinov and Suris's tight binding calculation[9] that, when the Wannier-Stark level splitting is smaller than the distance between the two lowest subbands of each quantum well of the superlattice, the electron is localized and the current through the structure is small. When both quantities are comparable, there is a peak in the current-field curve due to resonant tunneling between the first subband e_1 of one well and the second subband e_2 of the next one (let us denote by $e_1 \rightarrow e_2$ this kind of resonant tunneling). Further peaks correspond to other resonant transitions between different-energy subbands of the wells. As a result of resonant tunneling, electrons populate higher subbands of the wells and PL measurements may be used to probe the change of electron population in higher subbands.[3,4] In superlattices with wide wells the resonant tunneling process is sequential, which means that after a tunneling event the electrons decay very fast to a lower (e.g., the first) subband due to scattering.[10] For the superlattices described above, the intersubband scattering time is of the order of 1 ps, which is very small compared to the typical tunneling time of 500 ps.[11] When electric-field domains are formed, the wells belonging to each domain undergo similar sequential resonant tunneling (SRT) events. In Ref. 1 and previously in Ref. 4, three domains are observed for different bias and illumination: domain I where SRT is $e_1 \rightarrow e_1$ (the subbands of all the wells in this domain are aligned at zero electric field), domain II with $e_1 \rightarrow e_2$ SRT, and domain III with $e_2 \rightarrow e_3$ or $e_1 \rightarrow e_3$ SRT according to the sample. We have depicted schematically the SRT processes in a sample where domains II and III coexist in Fig. 1. Time-dependent PC oscillations are observed as a transient toward a stationary state where domains II and III coexist.[1]
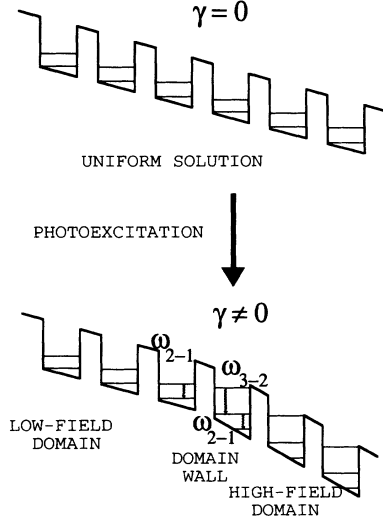
<u>50</u> 8644

FIG. 1. Different regions and processes that contribute to the PL spectrum (see text). Only the conduction band is represented.

In this paper we describe and analyze a simple discrete drift model that explains several features of the experiments reported in Ref. 1, particularly the stationary current-voltage characteristic curve[4] and the time-dependent oscillations of the PC in the region of the parameter space where domains II and III coexist. Previous theoretical works on electric-field domains in superlattices include Grahn et al.'s[4] characterization of stationary states, Laikhtman's equivalent circuit model,[12] and Korotkov et al.'s simulations based upon the analogy of a slim superlattice with a one-dimensional array of metallic tunnel junctions.[13] We shall comment on these works in the Discussion. To motivate our model let us consider several important time scales for the superlattices that are the object of our study. First of all, the characteristic time scale of the PC oscillations in Ref. 1 is 100 ns. The time scale for carrier thermalization is 0.1 ps, while the carriers reach thermal equilibrium with the lattice after a time that ranges from 1 to 100 ps.[14] This means that in time scales of the order of nanoseconds (the experimental time scale), we may consider the holes and electrons to be at local equilibrium within each quantum well j at the lattice temperature, and with given values of their densities, $\tilde{p}_j$ and $\tilde{n}_j$. The process of reaching a stationary state might be seen as the attempt to reach a "global equilibrium" starting from "local equilibrium" through tunneling processes that connect different quantum wells, self-consistency of the electric field, and scattering and interband processes. In this spirit we consider the quantum wells as entities characterized by average values of the electric field, $\tilde{E}_j$ for the jth well, and of the densities of holes and electrons, $\tilde{p}_j$ and $\tilde{n}_j$, respectively. We then propose the following transport equations to describe the dynamics of the superlattice:

$$\tilde{E}_j - \tilde{E}_{j-1} = \frac{e\tilde{l}}{\epsilon}\,(\tilde{n}_j - \tilde{p}_j), \qquad (1.1)$$

$$\epsilon\,\frac{d\tilde{E}_j}{d\tilde{t}} + e\tilde{v}(\tilde{E}_j)\,\tilde{n}_j = \tilde{J}, \qquad (1.2)$$

$$\frac{d\tilde{p}_j}{d\tilde{t}} = \tilde{\gamma} - \tilde{r}\,\tilde{n}_j\,\tilde{p}_j, \qquad (1.3)$$

where $j = 1,\ldots,N$. In this model, the equations mean the following.

(1) Equation (1.1) is the discrete Poisson equation relating the field at two adjacent wells and the electric charge; e is the electron charge, $\tilde{l}$ is the length of one period of the superlattice, and ϵ is an average permittivity. Equation (1.1) may be considered as the average of the usual Poisson equation over one period of the superlattice. Since the heterostructure corresponds to an intrinsic semiconductor, we do not include charged impurities in (1.1). Poisson's equation for the $j = 1$ well contains the field at the "zeroth" well, which corresponds to the doped semiconductor before the superlattice and it will be dealt with below.

(2) Equation (1.2) is Ampère's law at the jth well establishing that the total current density $\tilde{J}$ is the sum of the displacement current and the electron flux. We consider that the holes are heavy and their contribution to the current is negligible.[15] The electron flux $J^T_{j \to j+1} = e\tilde{v}(\tilde{E}_j)\,\tilde{n}_j$ is due to sequential resonant tunneling between subbands of neighboring quantum wells as said above. By writing this expression we are assuming that the probability of tunneling from the well j to the well $j + 1$ is proportional to the number of electrons in the well j, and we are ignoring the small "reverse tunneling" from the well $j + 1$ to the well j. The probability of tunneling is larger for fields corresponding to SRT (for which the subband e_1 of j is aligned with e_2 of $j + 1$, or e_2 of j with e_3 of $j + 1$, etc.). This implies that the function $\tilde{v}(\tilde{E})$ (with the dimensions of a velocity) has peaks at the corresponding values of the electric field. A crucial assumption of our model is that the electron "velocity" corresponds to the static current-voltage characteristic of the superlattice at low laser power [small $\tilde{\gamma}$; see (1.7) below]. We take this curve as a datum of our model and argue that our results do not depend qualitatively on the exact shape of $\tilde{v}(\tilde{E})$. Since we are interested in the analysis of the region where domains II ($e_1 \to e_2$ SRT) and domains III ($e_2 \to e_3$ or $e_1 \to e_3$ SRT) coexist, we have used a velocity curve with two local maxima centered in the same field values as seen in the experiments.[1,4] The result is Fig. 2. To explore the region where domains I ($e_1 \to e_1$ SRT) and II coexist, it is convenient to add another (smaller) peak to the velocity curve at zero electric field. The modifications will be reported elsewhere.

(3) Equation (1.3) is the rate equation for the hole concentration. We consider only processes of photogeneration of electron-hole pairs and recombination. The photogeneration term $\tilde{\gamma}$ is proportional to the power of the laser (Ref. 16, Chap. 12; see also Delalande's paper in Ref. 17), which we assume (for simplicity) illuminates the superlattice uniformly. The recombination coefficient is assumed to be constant.

Notice that the rate equation for the electrons containing the photogeneration, recombination, and SRT processes is
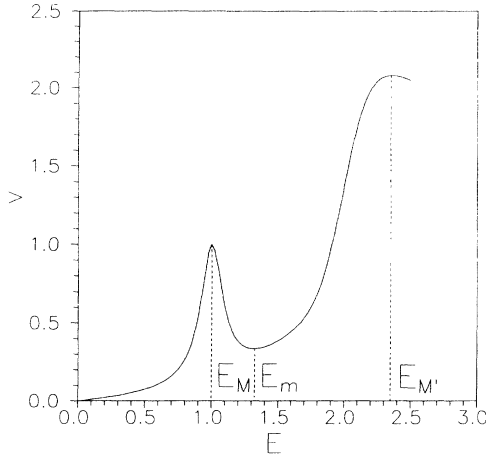
FIG. 2. Dimensionless velocity of the electrons as a function of the electric field. It is modeled by two Lorentzians centered at E_M and $E_{M'}$ which correspond to the sequential resonant tunneling current between the quantum wells j and $j + 1$. At a field E_M, there is SRT between the first level of the jth well and the second level of the $(j+1)$th well, whereas at a field $E_{M'}$ there is SRT between the second level of the jth well and the third level of the $(j + 1)$th well. [In different samples, the latter SRT process may relate the first level of the jth well and the third level of the $(j + 1)$th well.]

$$\frac{d\tilde{n}_j}{d\tilde{t}} = \tilde{\gamma} - \tilde{r}\tilde{n}_j\tilde{p}_j + \frac{1}{\tilde{l}}\{\tilde{v}(\tilde{E}_{j-1})\tilde{n}_{j-1} - \tilde{v}(\tilde{E}_j)\tilde{n}_j\}. \quad (1.4)$$

Here the SRT current coming from well $j - 1$ to well j brings electrons to the jth well at a rate $\tilde{v}(\tilde{E}_{j-1})\,\tilde{n}_{j-1}/\tilde{l}$, while the SRT current going from well j to well $j + 1$ subtracts electrons from the jth well. This equation is equivalent to (1.2), as can be shown by differentiating (1.1) and using (1.2) and (1.3).

In the $3N$ equations (1.1)–(1.3) there are $3N + 2$ unknowns, $\tilde{J}$, $\tilde{E}_0, \tilde{E}_j, \tilde{n}_j, \tilde{p}_j$, with $j = 1, \ldots, N$. One additional equation is the bias condition

$$\frac{1}{N} \sum_{j=1}^{N} \tilde{E}_j = \frac{\tilde{\Phi}}{N\tilde{l}}. \quad (1.5)$$

Here $\tilde{\Phi}$ is the difference between the applied voltage and the built-in potential due to the doped regions outside the superlattice (1.5 V in Ref. 1). $\frac{\tilde{\Phi}}{N\tilde{l}}$ is the average applied electric field on the superlattice, which we will henceforth call the *bias*. The missing condition is a boundary condition for the field at the zeroth well, $\tilde{E}_0$ (*before* the superlattice). We do not have direct experimental evidence for what $\tilde{E}_0$ should be. Thus our choice for $\tilde{E}_0$ has to be validated *a posteriori* by comparing the results of our analysis with experiments and with the consequences of a different choice. We shall use throughout this paper the following boundary condition:

$$\tilde{E}_0(\tilde{t}) = \tilde{E}_1(\tilde{t}). \quad (1.6)$$

This condition does not allow a charge build-up at the first well and it is compatible with the experimental observation that the field is the same for all the wells at low laser power:

$$\tilde{v}\left(\frac{\tilde{\Phi}}{N\tilde{l}}\right) = \frac{\tilde{J}\tilde{r}^{1/2}}{e\tilde{\gamma}^{1/2}}, \quad \tilde{E}_j = \frac{\tilde{\Phi}}{N\tilde{l}}, \quad (1.7)$$

for all j. This equation says that the effective electron velocity is (except for constant scale factors) the same as the static I-V characteristic curve of the superlattice at low laser power, which allows us to infer the form of $\tilde{v}(\tilde{E})$ from experimental data. Thus our boundary condition (1.6) forces a uniform field profile (the same $\tilde{E}_j$ for all j) to be a solution of our model for any laser power. As we shall see later, this uniform solution is stable for low laser power whereas the model subject to the same boundary condition (1.6) may have stable nonuniform field profiles (with domains) for large enough laser power. Further discussion of the boundary condition is postponed to Sec. VI. For the velocity curve $\tilde{v}(\tilde{E})$, we have used a variety of phenomenological curves with two peaks and a negative-differential resistance (NDR) region of negative slope between them. We could also have obtained the velocity curve from microscopic theories of static I-V curves for superlattices but, given the qualitative insensitivity of our results to variations of the velocity curve (as we will explain later), we have stuck to curves with easy analytical expressions for the calculations presented here.

The boundary condition (1.6) allows for electric field domains E_j, $j = 1, \ldots, N$ made of two constant values of the electric field and a domain wall connecting them, as we shall discuss below. The fact that our superlattice is embedded in a p-i-n diode implies that domains with low field at $x = 0$ and high field at $x = L$ are preferred to domains with the symmetric configuration [see Eq. (1.1)]. Thus we shall only consider initial conditions that favor this kind of electric-field domain and we will not mention the domains that start at $x = 0$ with high electric field, even though they may be possible with our boundary condition. When the superlattice forms part of a different diode, e.g., n-i-n, the two kind of domains are allowed and richer structures may arise according to the initial condition used in the simulations.

It is convenient to render dimensionless the equations of our model before we proceed to their analysis. For this, we adopt as the unit of electric field that at the first maximum of the velocity curve $\tilde{E}_M \simeq 10^5$ V/cm. Then (1.1) yields the typical unit of electron density,

$$\tilde{n} = \frac{\epsilon\tilde{E}_M}{e\tilde{l}} \simeq 10^{18}\,\mathrm{cm}^{-3}, \quad (1.8)$$

for $\tilde{l} \simeq 100$ Å. There are two important time scales in our model. From (1.2) we see that the electrons employ a time $\tau_e = \tilde{l}/\tilde{v}(\tilde{E}_M) \simeq 0.5$ ns to tunnel from one well to the next one of the superlattice. From (1.3), we find the time scale in which the hole density varies,

$$\frac{1}{\tau_p} = \tilde{r}\tilde{n}. \quad (1.9)$$

Thus τ_p is essentially given by the recombination coefficient $\tilde{r}$. $\tilde{r}$ is a decreasing function of the electric field because the overlap between the electron and hole wave functions decreases as the field increases.[18] This accounts for a variation of τ_p from subnanoseconds to tens of nanoseconds.[18] Here we adopt $\tau_p = 10$ ns which is reasonable in view of the experimental values reported in Ref. 1. We measure the time in units of τ_p which together with the previously mentioned units completes the following definition of dimensionless variables:

$$E_j = \frac{\tilde{E}_j}{\tilde{E}_M}, \quad p_j = \frac{\tilde{p}_j}{\tilde{n}}, \quad n_j = \frac{\tilde{n}_j}{\tilde{n}},$$

$$t = \frac{\tilde{t}}{\tau_p} = \tilde{r}\tilde{n}\tilde{t}, \quad J = \frac{\tilde{J}}{e\,\tilde{n}\,\tilde{v}(\tilde{E}_M)}, \tag{1.10}$$

and parameters

$$\phi = \frac{\tilde{\Phi}}{\tilde{E}_M\,N\tilde{l}}, \quad \gamma = \frac{\tilde{\gamma}}{\tilde{r}\tilde{n}^2}, \quad \beta = \frac{\tau_e}{\tau_p} = \frac{\tilde{r}\tilde{l}\tilde{n}}{\tilde{v}(\tilde{E}_M)}. \tag{1.11}$$

Inserting (1.10) and (1.11) into (1.1)–(1.6) we find the dimensionless system

$$E_j - E_{j-1} = n_j - p_j, \tag{1.12}$$

$$\beta \frac{dE_j}{dt} + v(E_j)\,n_j = J, \tag{1.13}$$

$$\frac{dp_j}{dt} = \gamma - n_j\,p_j, \tag{1.14}$$

$$\frac{1}{N} \sum_{j=1}^{N} E_j = \phi, \tag{1.15}$$

$$E_0 = E_1. \tag{1.16}$$

Here β goes from 0.01 to 1 and ϕ and γ are the dimensionless control parameters. These equations are to be solved with initial conditions for the fields $E_j(0)$ and the hole concentrations $p_j(0)$ compatible with the bias (1.15) and the boundary condition (1.16). The initial conditions for the electron density $n_j(0)$ then follow from (1.12).

II. STEADY STATES

For given values of γ and J there are stationary solutions of Eqs. (1.12)–(1.14) compatible with the boundary condition (1.16). Using Eq. (1.15), we find the corresponding value of ϕ. From this we can obtain the curves $J = J(\phi)$ appearing in Fig. 3. We have studied two different types of stationary solutions, namely, uniform solutions and two-domain solutions.

A. Uniform solutions

By inserting $E_j \equiv E$ (constant) into (1.12)–(1.15), we find

$$E = \phi, \tag{2.1}$$

$$n_j = p_j = \sqrt{\gamma} \qquad (j = 1, \ldots, N), \tag{2.2}$$

$$J = \sqrt{\gamma}\,v(\phi). \tag{2.3}$$

Equation (2.3) yields a static current-voltage characteristic curve which is the same as $v(E)$ except for a scale factor (see Fig. 3).

B. Nonuniform two-domain solutions

The stationary versions of Eqs. (1.13) and (1.14) can be solved for n_j and p_j in terms of the electric field E_j and then inserted in (1.12). The result is the following discrete mapping:

$$E_{j-1} = f(E_j; \gamma, J), \tag{2.4}$$

with

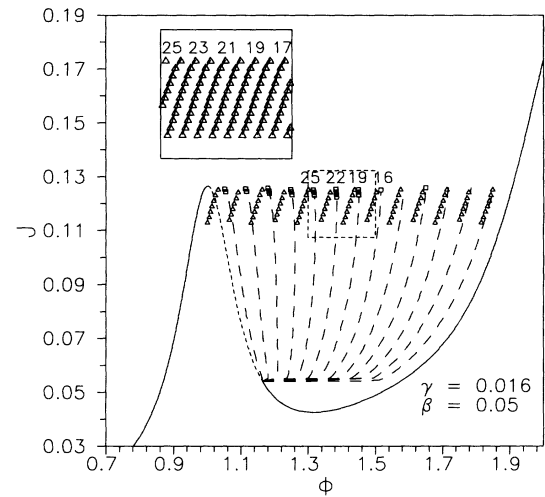$$f(E; \gamma, J) \equiv E - \frac{J}{v(E)} + \frac{\gamma}{J}\,v(E). \tag{2.5}$$

FIG. 3. Static characteristic curve: current (J) versus applied bias (ϕ) for laser power $\gamma = 0.016$ (β, which is only relevant for the stability of the different solutions [see (A2) in the Appendix], is assumed to be 0.05). The solid line corresponds to the stable uniform solution. In the NDR part of the curve there is a region where this solution becomes unstable (short-dashed line). The remaining curves correspond to two-domain solutions. There are 39 branches (one less than the number of quantum wells), though only one of every three branches has been plotted for the sake of clarity. The inset enlarges a small region of the figure showing the branches in full detail. Each branch has a different number of wells (from 1 to 39) in the low-field domain (the number written on top of some of them). Every branch consists of two curves, according to the way they are built with the discrete mapping (2.4) (see text for details): one plotted with triangles, corresponding to jumps from the first to the third fixed points of (2.4), and another plotted with a combination of squares (stable part) and long dashed lines (unstable part), corresponding to jumps from the second to the third fixed points of (2.4). Important features to stress from this figure are first, the coexistence, for a given ϕ, not only of several domain solutions but also of domain solutions and the uniform solution (see also Fig. 5), something relevant to the appearance of hysteresis and memory effects, and second, the average "flatness" of J in the bias region between the two local maxima of $v(E)$.

The mapping (2.4) allows us to get all the electric-field profiles $\{E_j, \; j = 1, \ldots, N\}$ that satisfy the boundary condition $E_0 = E_1$. From these profiles and the bias condition (1.15), we obtain the current-voltage characteristic curve of Fig. 3. Motivated by experiments, we are interested in stationary solutions with two electric-field domains, i.e., $E_j = E_L$ (E_L is the constant low-field value) for $j = 1, \ldots, k$; $E_j = E_H$ (E_H is the constant

high-field value) for $j = N - \tilde{k} + 1, \ldots, N$, whereas for the remaining quantum wells ($j = k + 1, \ldots, \tilde{k}$) E_j is an increasing function of j that takes values on the interval (E_L, E_H). These wells constitute the domain wall that separates domains II and III.

For these solutions to exist, a few requirements have to be fulfilled. First of all, the boundary condition (1.16) together with (2.4) implies that E_0 should be a fixed
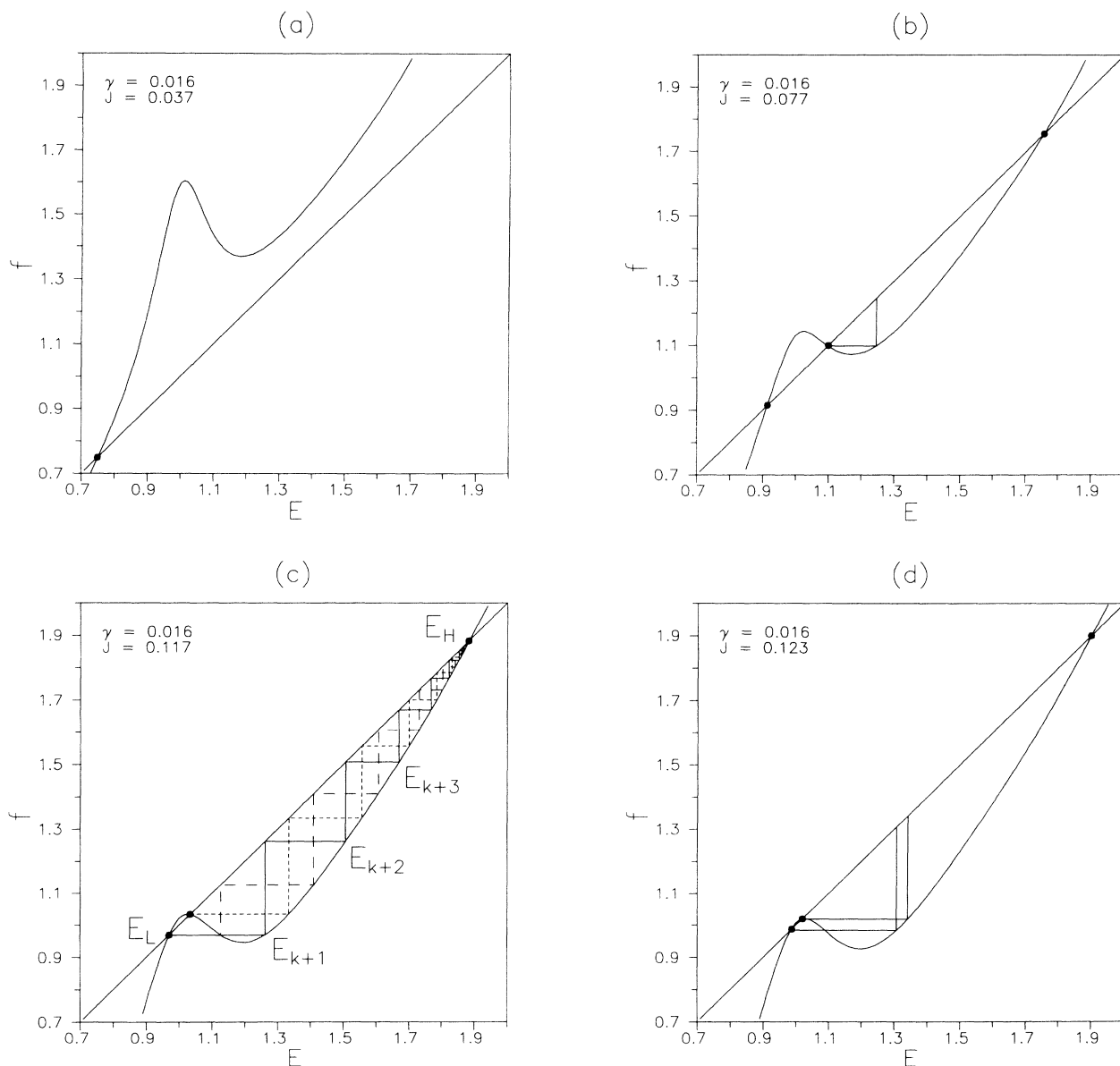

FIG. 4. The discrete mapping: $f(E; \gamma, J)$ and E versus E for $\gamma = 0.016$ and five different values of J. (a) For small J [below the minimum of $\sqrt{\gamma}\, v(E)$], only one fixed point of the discrete mapping appears; thus only uniform solutions are allowed. (b) There are three fixed points of the discrete mapping, but only $2 \to 3$ jumps are allowed. (c) Now both $1 \to 3$ and $2 \to 3$ jumps are allowed. The continuous lines show the discrete mapping process used to construct a ($1 \to 3$) nonuniform stationary solution with two domains. After remaining at the low-field domain value E_L, the field jumps at the $(m+1)$th well to a different solution of $f(E; \gamma, J) = E_L$. In successive iterations the electric field tends to its high-field value E_H. The short-dashed lines show the same construction for a $2 \to 3$ solution, whereas the long-dashed lines correspond to a different (unstable) type of $2 \to 3$ solution explained in the text. (d) Same as (c), but showing the coalescence of solutions with $1 \to 3$ and $2 \to 3$ jumps for $J = \sqrt{\gamma}\, v(E_M)$. (e) For large J, above the first positive maximum of $\sqrt{\gamma}\, v(E)$, there is only one fixed point of the discrete mapping and the situation is the same as in (a): the only possible stationary solutions are uniform.
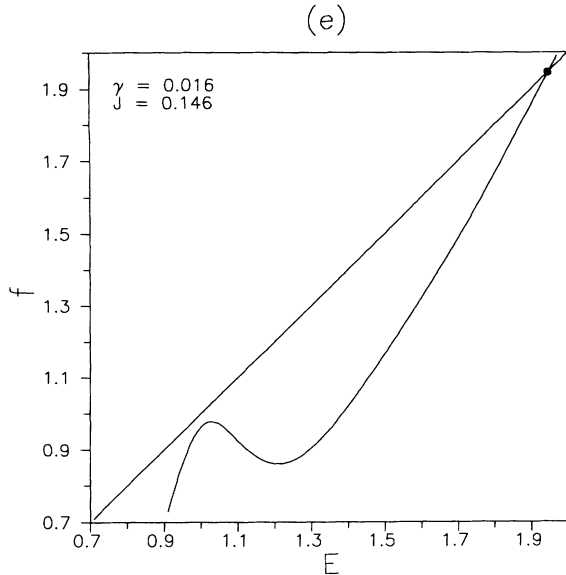
(e)

FIG. 4. *(Continued)*.

point of the discrete mapping (2.4), i.e., a solution of

$$f(E; \gamma, J) = E \qquad (2.6)$$

(see Fig. 4). Furthermore in order to have a nonuniform solution with domains, (2.6) should have more than one fixed point. After simplification, Eq. (2.6) becomes (2.3) and therefore this requirement is satisfied for certain values of J described below. Let E_L be the fixed point of the mapping that we choose for E_0. With the $v(E)$ profile depicted in Fig. 2, (2.6) may have one or three solutions depending on the values of J and γ. Let E_M, $E_{M'}$, and E_m be the positive electric field at the first and second positive maximum and at the first positive minimum of $v(E)$, respectively (see Fig. 2). For $0 < J < \sqrt{\gamma}v(E_m)$ and for $\sqrt{\gamma}v(E_M) < J < \sqrt{\gamma}v(E_{M'})$, (2.6) has only one solution on the interval $(0, E_{M'})$. For $\sqrt{\gamma}v(E_m) < J < \sqrt{\gamma}v(E_M)$, there are three solutions of (2.6) on the same interval. Thus we can find a fixed point E_L on the interval $(0, E_{M'})$ for $0 < J < \sqrt{\gamma}v(E_{M'})$. Secondly, a nonuniform profile should have $k < N$ wells with fields equal to E_L and $E_{k+1} > E_L$. This means that the equation

$$f(E; \gamma, J) = E_L \qquad (2.7)$$

should have at least a solution different from the fixed point, otherwise only the uniform solution described above is possible. This second condition holds only for $\gamma > \gamma_1 \simeq 5.2 \times 10^{-3}$ (see Sec. III). If one of the two lowest fixed points of (2.4) satisfies these two conditions, we can select it as the value of the low-field domain E_L and let the k first wells have this value for their electric fields ($E_j = E_L$, $\forall j = 1, \ldots, k$). Then one may choose as E_{k+1} another solution of (2.7) different from E_L. The p-i-n character of the diode prescribes that this is an acceptable solution provided the electric field E_{k+1} is higher than E_L. Then (2.4) implies that E_j increases

with j and approaches another fixed point, which is the value E_H of the high-field domain. As Fig. 4 shows, for each fixed $\gamma > \gamma_1$ both conditions are satisfied only for values of J on a certain interval and for some of the fixed points of the mapping. The current-applied bias (J-ϕ) characteristic curves obtained with the previously described method are depicted in Fig. 3 for $\gamma = 0.016$. As explained before, the continuous curve (together with the short-dashed part in the NDR region) is $\sqrt{\gamma}v(\phi)$, with $v(E)$ depicted in Fig. 2. It corresponds to the uniform solution, obtained when all the E_j stay on one of the fixed points (2.6). The J-ϕ curves for the nonuniform stationary solutions with two domains explained above appear for ϕ on an interval that ranges from a value slightly below E_M to a value slightly below $E_{M'}$ in Fig. 3. They exist for $\gamma > \gamma_1$ and J on a subinterval of $(\sqrt{\gamma}v(E_m), \sqrt{\gamma}v(E_M))$ whose width increases with γ.

Let us now describe several important nonuniform stationary profiles of the electric field. Consider in the first place the curves formed by small triangles in Fig. 3. They correspond to nonuniform solutions with $E_j = E_L$ [the first fixed point of the discrete mapping on the first branch of $v(E)$] for $1 \leq j \leq k$ (the number k is shown on top of several such curves in Fig. 3). For $j > k$, E_j "jumps" to the third branch of $f(E; \gamma, J)$ and it approaches the third fixed point of the discrete mapping ($1 \to 3$ jumps); see these iterations of the discrete mapping in Fig. 4(c) for a typical value of J. As ϕ increases and k decreases, each branch in Fig. 3 corresponds to the same steady field profile but with the domain wall displaced one step backward (towards $x = 0$), which means that a new quantum well has lost the low-field value. In the main body of Fig. 3, only one out of each three branches of stationary profiles of this type is depicted. The inset shows all these solution branches for k between 17 and 25. Since they turn out to be linearly stable (see the Appendix), multistability between different stationary profiles corresponding to the same voltage ϕ is possible. As γ grows, the width of the J interval for which these solutions exist increases, and so does the length of the triangle curves in Fig. 3. Then coexistence of *more* than two stable stationary field profiles for the same ϕ is possible. This gives rise to larger hysteresis cycles and memory effects. When do the stationary field profiles with $1 \to 3$ jumps exist? As the sequence of Figs. 4(a)–4(c) shows, the values of γ and J should allow the local minimum of $f(E; \gamma, J)$ to descend below the first fixed point of the mapping. This is possible for $\gamma > \gamma_1$ and $J \in (J_1(\gamma), \sqrt{\gamma}v(E_M))$, where the minimum of $f(E; \gamma, J)$ coincides with the first fixed point at the current $J_1(\gamma)$. The branches of stationary solutions with $1 \to 3$ jumps end at $J = \sqrt{\gamma}v(E_M)$ when the fixed points on the first and second branches of the discrete mapping coalesce and disappear.

Consider now the curves with small squares (and their long-dashed continuations) in Fig. 3. They correspond to stationary solutions with $E_j = E_L$, which is now the second fixed point of the discrete mapping, for the first k quantum wells. For $j > k$, E_j jumps to the third branch of $f(E; \gamma, J)$ ($2 \to 3$ jumps). The short-dashed lines in Fig. 4(c) represent the iterations of the discrete

mapping leading to one of these solutions. For a given γ, for which range of J do the stationary field profiles with $2 \to 3$ jumps exist? We shall argue (and have checked numerically) that the profiles with $2 \to 3$ jumps exist for $J \in (J_2(\gamma), \sqrt{\gamma}\, v(E_M))$, where $J_2(\gamma)$ is determined from (2.3) and (2.8) below. From Fig. 4(b) we see that these profiles appear at a value of $J = J_2(\gamma)$ where the slope of $f(E; \gamma, J)$ at the second fixed point of the mapping is zero. We observe in Fig. 3 that all $2 \to 3$ solution branches taper down to a point[19] $\phi_2(\gamma)$ for $J = J_2(\gamma)$. We find $\phi_2(\gamma)$ and $J = J_2(\gamma)$ by inserting (2.3) into the condition that the slope of $f(E; \gamma, J)$ be zero:

$$v + 2\sqrt{\gamma}\, v' = 0. \tag{2.8}$$

This equation has one solution corresponding to the minimum of $f(E; \gamma, J)$ which determines $\phi_2(\gamma)$. Substituting $\phi_2(\gamma)$ into (2.3) we obtain $J_2(\gamma)$. The smallest possible γ for which (2.8) has solutions is $\gamma = \gamma_1 \simeq 5.2 \times 10^{-3}$: nonuniform stationary profiles exist for $\gamma > \gamma_1$. As we indicate in the Appendix, the curve (2.8) bounds the region inside which the uniform stationary solution is linearly unstable. As in the case of the stationary field profiles with $1 \to 3$ jumps, only one out of three branches corresponding to profiles with $2 \to 3$ jumps is depicted in Fig. 3. Clearly many more stationary solutions can be constructed with the help of the discrete mapping, and we have depicted only the more significant ones in Fig. 3. We want to point out that all the stationary branches are connected: they do not disappear as could be wrongly inferred from our Fig. 3. For example, in Fig. 4(c) we have shown (long-dashed line) the mapping corresponding to a stationary field profile different from the pure $1 \to 3$ (continuous lines) and $2 \to 3$ (short-dashed lines) jumps. For these (unstable) solutions, E_{k+1} jumps to the *second* branch of $f(E; \gamma, J)$ (instead of jumping directly to the third branch) before continuing toward the third fixed point of the mapping. Clearly, the branches corresponding to these solutions coalesce with the $1 \to 3$ branches at $J = J_1(\gamma)$ and explain the disappearance thereof.

We have found stable nonuniform stationary states having two domains with electric fields E_L and E_H separated by a domain wall. These fields are (i) $E_L < E_M$ (curves formed by small triangles in Fig. 3) or $E_L \in (E_M, E_m)$ (curves formed by small squares in Fig. 3), and (ii) $E_H \in (E_m, E_{M'})$.

Thus while the first domain may have an electric field below or above the SRT value E_M, the field at the second domain is always below the second SRT value $E_{M'}$. Notice that this happens independently of the applied bias for $\phi \in (E_M, E_{M'})$. That the field at the domains does not necessarily coincide with the field for which there is resonant tunneling is in agreement with experimental observations[1] and previous theories.[12] For applied bias on $(E_M, E_{M'})$, the average of the stationary current at the branches representing non-uniform states is independent of the bias, which explains the "flat" shape in Fig. 3. The experimental data present both flat plateaus and rising profiles in the I-V characteristic curves of the samples.[1,4]

III. LASER POWER VS APPLIED BIAS "PHASE DIAGRAM"

With the aim of interpreting the experimental results, we have to delimit the intervals of the parameters γ and ϕ where stable solutions of the types described in the preceding section may be found. A discussion of their linear stability is postponed to the Appendix, but this information together with that provided by the discrete mapping of the preceding section allows us to draw the γ-ϕ "phase diagram" of Fig. 5. The continuous line in Fig. 5 bounds the region in which stable nonuniform solutions with domains exist. The flat bottom of this region is at $\gamma = \gamma_1$, the photoexcitation below which nonuniform stationary states do not exist. The continuous line in Fig. 5 has been obtained numerically by the following procedure.

From Fig. 3 we see that the branches of stable nonuniform solutions that yield the minimum and maximum values of ϕ are the two extreme small triangles. We have used the discrete mapping (2.4) to find with precision those extreme values of ϕ as functions of γ. For a given γ, the range of J for which the discrete mapping (2.4) allows for stable nonuniform solutions of any type (with $1 \to 3$ or $2 \to 3$ jumps) has been determined following the procedure explained in Sec. II. Notice that the minimum value of ϕ (in the continuous line of the phase diagram Fig. 5) is determined by taking the smallest $J = J_1(\gamma)$ for which it is possible to find a solution of (2.4) and (1.16) having 39 wells with field E_L at the lowest fixed point and one well with a higher electric field. On the other side, the maximum value of ϕ on the continuous line of Fig. 5 is reached at the end of the last small triangle branch of Fig. 3. This value of ϕ is found by letting $E_0 = E_1 = E_L$ be the second fixed point of (2.4) at $J = \sqrt{\gamma}\, v(E_M)$ [the value of J for which the two first fixed points of (2.4) coincide] and then using (2.4) to find the other values
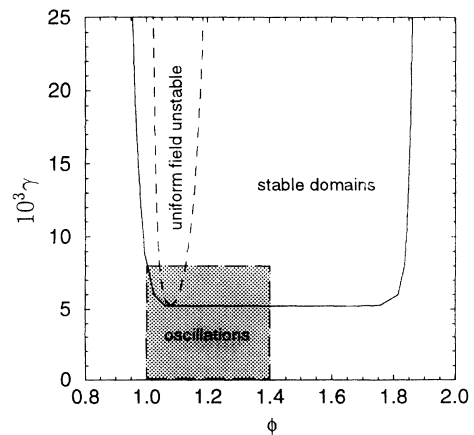

FIG. 5. Phase diagram of the model: laser power (γ) vs voltage bias (ϕ). Stable nonuniform solutions with domains exist only inside the continuous curve. Inside the dashed line the uniform solution is unstable. The shaded rectangle approximately delimits the region where oscillations of the PC (i.e., of the domain wall of the electric-field profile) can be obtained.

$E_j > E_L$ with $j > 1$.

Inside the continuous line in Fig. 5 we have depicted with a dotted line the curve (2.8). As we explain in the Appendix, the uniform solution is linearly unstable inside this curve. Between both curves in Fig. 5, both the uniform solution and at least one branch (often several) of nonuniform solutions are linearly stable for a given value of ϕ. As discussed in Sec. II, we can easily visualize multistability with the help of Fig. 3.

IV. SIMULATION

From the experiments we have information about the *steady state* of the problem through the current-voltage characteristics, and about the *dynamical* aspects thereof through the time evolution of the PC and of the PL. In our model we have direct access to the time evolution of the PC, proportional to $J(t)$, while we would need to supplement our model to be able to obtain the time evolution of the PL. We shall consider the evolution of the $J(t)$ and of the electric field and charge profiles in this section, while we will give qualitative arguments about the evolution of the PL in the next section.

In the previous stationary study we have found a very rich γ-ϕ phase diagram, showing multistability and hysteresis. We have seen that our model accounts in a very satisfactory way for the static properties observed experimentally. The picture will be substantially completed by describing the time evolution of solutions of our model, which will explain most of the dynamical experimental results associated with the PC.[1] To extract time-dependent magnitudes from our model we have solved numerically the system of first-order nonlinear equations, by. means of a standard fourth-order Runge-Kutta method. For a fixed value of voltage and laser power we turn on the laser at $t = 0$. The initial conditions for the fields and the charge carriers are Eqs. (2.2) and (2.1), except that we increase the charge at the first quantum well to mimic the effect of the laser, and then let the system evolve according to Eqs. (1.12)–(1.16).

The analysis of the steady states in Sec. II reveals that at low laser power $\gamma < \gamma_1$ ($\simeq 5.2 \times 10^{-3}$ in our rescaled parameters), there is only one steady solution, the uniform one, (2.2) and (2.1), which is linearly stable (to be more precise, the same is true for the whole region outside the full line of the γ-ϕ phase diagram shown in Fig. 5). This result confirms the usual assumption that the PC at low power laser is just a rescaled plot of the velocity of the electrons versus the electric field,[20] and supports our choice of boundary conditions. Above this threshold there is always a voltage interval (inside the full line in Fig. 5) where multiple steady states exist. These states have steplike electric-field profiles as described above and some of them are linearly stable (see Fig. 3). These solutions may even coexist with the uniform one, which is unstable only inside the dotted line in Fig. 5.

Nevertheless, from a dynamical point of view, the simulations reveal an interesting behavior in the laser power range $0 < \gamma < \gamma_2$ ($\simeq 8 \times 10^{-3}$) for ϕ on a subinterval of $(E_M, E_{M'})$ (for $\gamma = 0.016$, $1 \leq \phi \leq 1.4$; see Fig. 5). The situation may be described as follows.
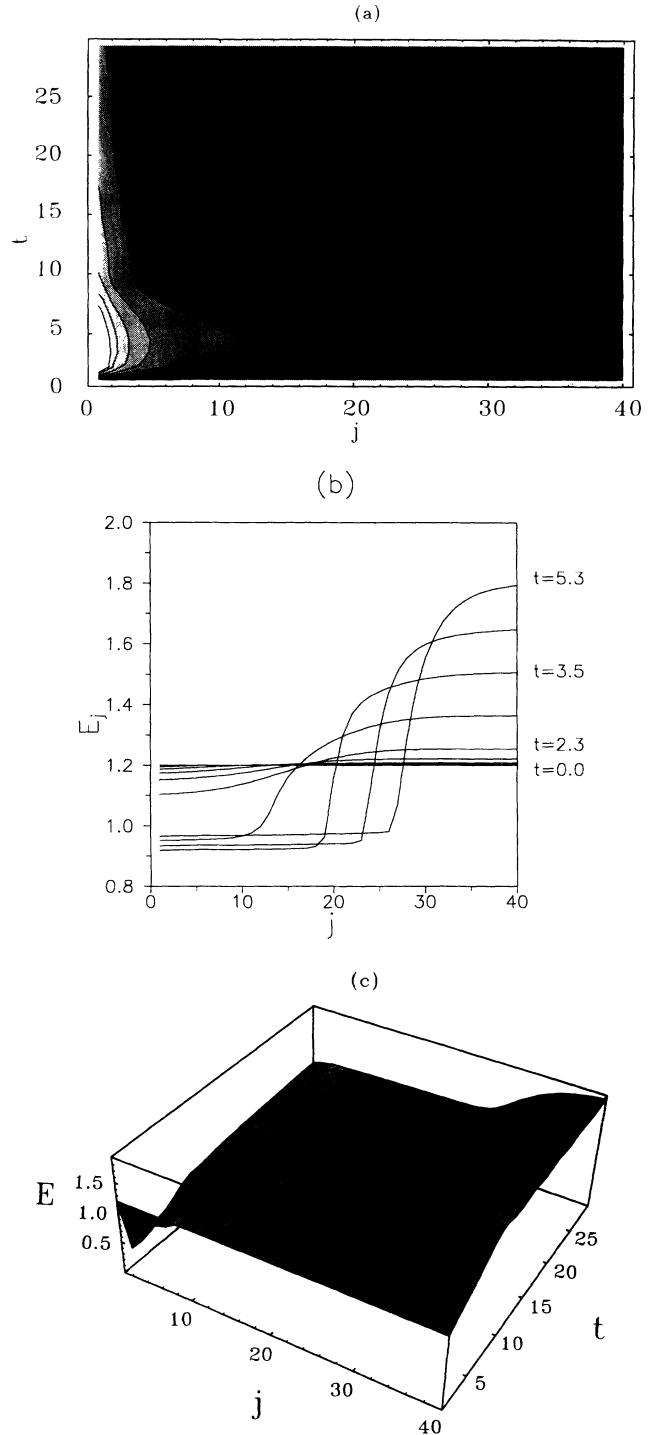

(a)

(b)

(c)

FIG. 6. Evolution of the domain wall in time for $\gamma = 2 \times 10^{-3}$ and $\phi = 1.2$. (a) is a contour plot with time flowing on the y axis and the quantum well number on the x axis. The electric-field contours go from 0.5 to 1.7 in 0.1 steps. At $t = 0$ we start with the uniform solution. The perturbation is clearly visible at the first well at short times. The creation and the displacement of the domain wall can be visualized. At $t = 0.5$ the two domains are already defined (the darker the figure the higher the electric field) and the domain wall begins to oscillate. Most of the wells have an electric field centered around the first maximum of $v(E)$ (low-field domain). In (b) we represent the electric-field profile at short times (domain formation) and in (c) the domain wall oscillations.

A. $0 < \gamma < \gamma_1$

There is only one steady state: that corresponding to a uniform profile of the electric field. The linear stability analysis reveals that this steady state is stable. However, if the disturbance is large enough, the numerical simulation shows that, after a short time, a non-steady steplike electric-field profile is formed. The domain wall of this profile oscillates back and forth in time about a fixed value of the position. As it oscillates, the domain wall changes its width, so that it spreads out over several wells, which makes easier the possibility of experimental detection. The electric field at the two domains in the profile also oscillates in time for a few periods before the oscillations stop (see Fig. 6 to visualize this process). Then there follows a very slow modification of the steplike profile which ends up in the uniform steady state. We call the steplike electric-field profile that remains after the PC oscillations cease the *metastable* state or the metastable domain formation. In Fig. 7, we have plotted the PC versus time for moderate and long times (inset), showing the oscillations and the final decay of the metastable state. Notice that the oscillations are appreciable only for $\gamma \geq 2 \times 10^{-4}$. Thus for $0 < \gamma < 2 \times 10^{-4}$ there is *overdamped* formation of a steplike field profile followed by a slow relaxation towards the uniform steady state.

B. $\gamma_1 < \gamma < \gamma_2$

There are true nonuniform steady states some of which are stable. The numerical simulations show a pattern analogous to that described above without the slow drift
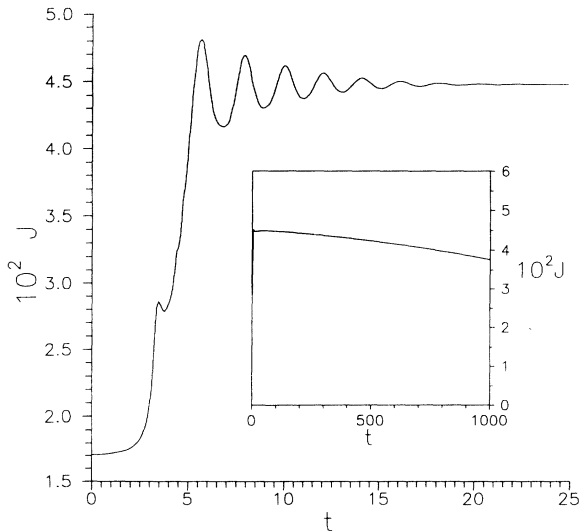

FIG. 7. The PC (J) evolution for the same values of the parameters as in Fig. 6. The transient before the oscillations corresponds to the formation of the low-field domain. The oscillations of the domain wall induce those of the PC. The maxima are reached when the domain wall is sharper. In the inset the small damping of the PC can be observed as the system slowly approaches the stable uniform solution. This damping disappears for large enough laser power (see text).
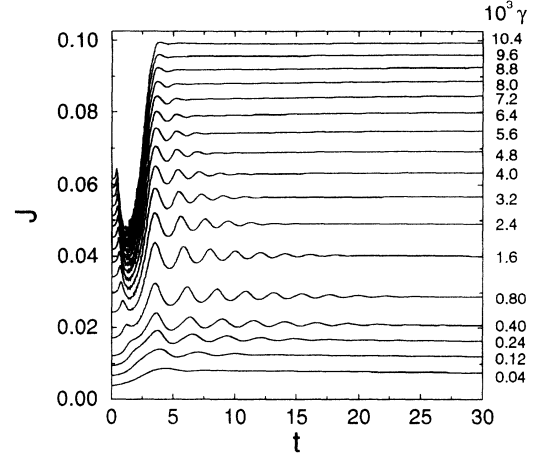

FIG. 8. Evolution of the PC J for different values of the photogeneration γ (in units of 10^{-3}), which increases from bottom to top of the figure, as indicated at the right margin. The voltage ($\phi = 1.1$) is the same for all the curves.

towards the uniform state: after the PC oscillations cease, a nonuniform steady state with two domains of the electric field is reached.

C. $\gamma > \gamma_2$

The damping is so strong that there are no oscillations of the PC: the steplike electric-field profile is reached in a monotonic fashion.

These results are visualized in Fig. 8 in which the evolution of the current with time is represented for increasing values of γ in a range that covers the three situations just described. The region of the phase diagram (Fig. 5) where oscillations — about either stable or metastable nonuniform solutions — can be observed has been represented by a dashed rectangle: $2 \times 10^{-4} < \gamma < 8 \times 10^{-3}$ and $1.0 < \phi < 1.4$, approximately. Outside this region, the damping about uniform or nonuniform (meta)stable steady states is so strong that no current oscillations may be observed. In Fig. 9 we have plotted the profiles of the electric field and of the electron and hole densities corresponding to a maximum and a minimum of the PC during one oscillation. Notice that the electronic charge oscillates from one side of the domain wall to the other during a period of the PC oscillation.[1] These results provide a clear picture of domain formation and posterior time evolution accounting for the time-dependent oscillations of the PC.

V. AN INTERPRETATION OF THE PL MEASUREMENTS

The PC discussed in the previous section gives integrated information about our sample, and is by no means a clear indication of domain formation. The experimental evidence of domain formation is the evolution in time
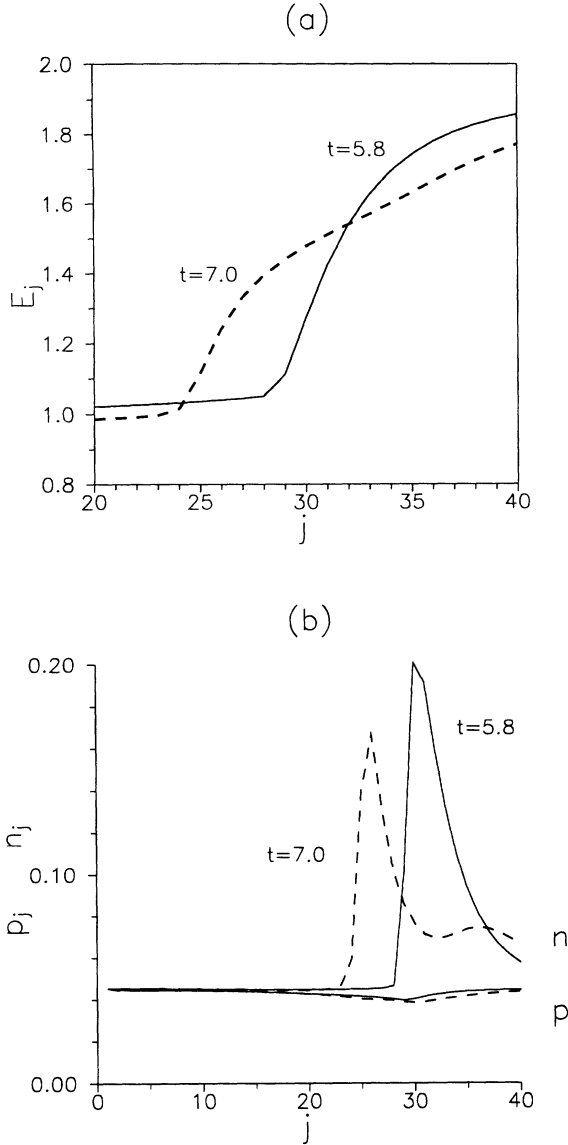
(a)

(b)

FIG. 9. (a) Electric-field profile and (b) charge at each well corresponding to a maximum (full line) and a minimum (dashed line) of the PC. Parameter values are the same as in Fig. 6.

of the PL spectrum, which measures the light emitted by the sample in the electron-hole recombination processes. Time-resolved PL is a direct way to measure the time evolution of the carrier distribution. A correct description of the PL spectra would require explicit consideration of recombination light emission, scattering, and tunneling times in the SRT process and of experimental resolution, which is out of the scope of the present work. However, we would like to supplement our model with a few assumptions so as to get a qualitative interpretation of the PL measurements. To do this, we need to understand the processes involved on the basis of the experimental information,[1] which can be summarized as follows.

(1) For large enough laser power and applied voltage, two PL peaks appear when the laser is switched on, confirming the formation of electric-field domains. Due to

the quantum confined Stark effect (QCSE)[21] we can affirm that the peak that appears at lower energy corresponds to higher value of the electric field than that at higher energy. The intensity of each peak is proportional to the number of electron-hole recombinations.

(2) As the applied voltage increases the intensity of the high-field peak (low energy) becomes greater but the position of the peaks remains approximately the same.

(3) The intensity of the peaks oscillates with time at the same frequency as the PC oscillations.

(4) The intensity of the low-field peak (high energy) is greater for a maximum of the PC than for a minimum and the reverse occurs for the high field.

The first two points indicate that the electric-field value at each domain does not vary as the applied voltage increases: the domain wall just moves toward the p contact, thereby increasing (decreasing) the size of the high- (low-) field domain. The third point shows that the electrons responsible for the PL are the same ones that carry the current across the sample.

All these points are highlighted in the following very simple formula which relates the PL spectrum, $I_{\mathrm{PL}}(\hbar\omega)$, to the carrier densities and the electric field at each well obtained from our model:

$$I_{\mathrm{PL}}(\hbar\omega) = \tilde{r}\sum_{j=1}^{N}\{\tilde{n}_j\,\tilde{p}_j\,\Delta(\hbar\omega - \Omega(\tilde{E}_j))\}. \qquad (5.1)$$

Here $\tilde{n}_j$ ($\tilde{p}_j$) is the electron (hole) concentration at the well j, $\tilde{r}$ is the recombination coefficient assumed to be field independent, and $\Omega(\tilde{E}_j)$ is the energy of the photon emitted in the recombination process at the jth well. Due to the QCSE, this energy depends on $\tilde{E}_j$, and it can be easily calculated with a one-well model.[22] The result shows an almost linear behavior of $\Omega(\tilde{E})$ with slope $2e\tilde{l}_w$ (e is the electron charge and $\tilde{l}_w$ is the width of the well). In (5.1), $\Delta(x)$ is just a Lorentzian function that counts the contribution of $\Omega(\tilde{E}_j)$ to the PL spectrum at energy $\hbar\omega$ with a finite resolution. In writing the expression (5.1) we have implicitly assumed that each well is at local equilibrium during the recombination process, as explained in the Introduction.

From Fig. 9 we see that a maximum of the PC occurs when the domain wall is almost vertical and the electric field at most of the wells takes on either the low- ($E_L \simeq E_M$) or the high- (E_H) field values, for which the tunneling probability is higher [cf. the curve $v(E)$]. During one oscillation, the low-field domain (which contributes to the high-energy peak in the PL spectrum) is larger at the maximum of the PC than at its minimum. According to (5.1) and our previous discussion, this should imply an increase in the low-field peak (high energy in the PL spectrum) for the maximum of the PC. When the PC takes on its minimum value within one oscillation, the domain wall is not so sharply defined and several quantum wells have a value of the electric field for which the tunneling probability is small.

The number of wells that are in the high-field (HF) domain increases with the applied voltage, and therefore, the weight of the low-energy peak (HF) increases with
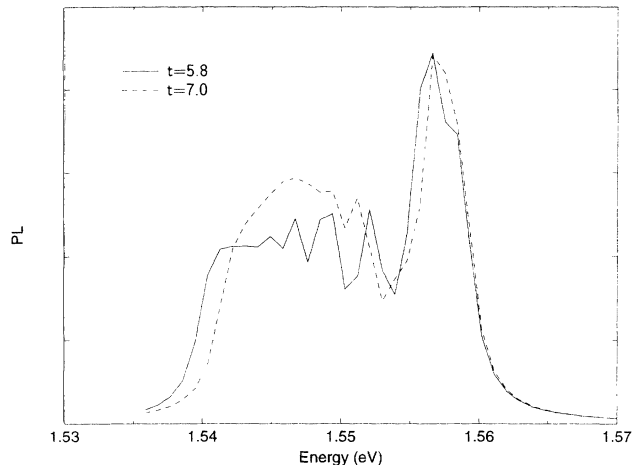
FIG. 10. Oscillations of the PL spectrum corresponding to Fig. 9.

the voltage, reflecting the growth of the HF domain. In Fig. 10 we show the PL spectrum for a maximum and a minimum of the PC for the same values as Figs. 6 and 9. The result resembles the experimental spectrum but it is clear that in order to get quantitative agreement a more elaborate model of the sequential resonant tunneling processes and electron-hole recombination is needed. This is out of the scope of the present work.

VI. DISCUSSION

We have analyzed a very simple model that addresses in a satisfactory way the transport aspects of the problem which are dominant at the time scales experimentally relevant[1] (1–100 ns): sequential resonant tunneling between weakly coupled quantum wells, photogeneration and recombination of electrons and holes, and self-consistency through the Poisson equation. An important aspect of our model is the *discrete* nature of its governing equations (1.12)–(1.15). Recall that this crucial feature is imposed by the separation between the relevant time scales of the above said transport processes and those of intra- and intersubband scattering (cf. Sec. I). Our results exhibit a wide variety of phenomena in agreement with the experiments: multistability of the stationary solutions with its consequences of hysteresis and memory effects,[4] time-dependent oscillations of the PC, domain and domain wall formation.[1] The metastability of the nonuniform stationary states predicted from our model is compatible with current experimental data, although longer observation times seem necessary for unambiguous confirmation.[1] Notice that the nonuniqueness of the stationary solutions is a direct consequence of our equations and it can be easily explained with the help of the multivalued discrete mapping of Sec. II. The nonuniform stationary field profiles exist on the interval of applied bias $(E_M, E_{M'})$ which is significantly *larger* than the NDR region (E_M, E_m). The region of multistability in the current-voltage characteristic curve is "flat" (the

average current does not change with the applied bias, Fig. 3). From our results it is clear that similar multistability due to coexistence between domains I (at zero field) and II (at field slightly below E_M)[4] may be obtained by adding a local maximum at zero field to the $v(E)$ curve. A simple modification of our Poisson equation and the equation for the holes may allow the study of similar phenomena in doped superlattices, which will be considered elsewhere.[23] It is important to notice that our results hold for a generic curve $v(E)$ of the form discussed in the paper and that we could fine-tune experimental data by changing the quantitative features of $v(E)$ and the parameter values. For instance, we could increase the size of the region where PC oscillations appear (long-dashed rectangle in Fig. 5) relative to $(E_M, E_{M'})$ by displacing the local minimum E_m towards $E_{M'}$. As there would be PC oscillations about nonuniform steady states with larger biases, the domain wall during a period of these oscillations would be closer to $x = 0$ than in Fig. 9. This would mean that we could obtain a larger domain III. In turn, this would cause a larger HF peak to appear in the PL spectrum of Fig. 10 thereby improving the agreement with experimental results.[1] Similarly the frequency of the PC time-dependent oscillations is an increasing function of β: We could estimate the ratio between the tunneling and recombination times by fitting the numerically obtained values of the frequencies to the experiments.

An important question, raised in the Introduction, is the dependence of our results on the boundary condition (1.6). Under this condition, the uniform stationary solution is stable at low laser power, which allowed us to identify the velocity curve with the I-V characteristic curve (except for unimportant constant scaling factors). At higher photoexcitation, the uniform stationary solution could become unstable in favor of nonuniform two-domain solutions, which agrees with the usual experimental interpretation.[4] All these facts are of course indirect evidence in favor of our choice (1.6). Still, one wonders whether other choices also yield results in agreement with the known facts. Without entering into detailed modeling of the contact and doped regions before the superlattice, one can consider other reasonable choices: it is plausible that modeling the region before the superlattice one obtains an increasing current-voltage curve (at least for not too large bias). Since E_0 is the average field before the superlattice, one could derive a formula $E_0 = g(J)$ from that current-voltage curve and use it as an alternative boundary condition instead of (1.6). Under this new condition we can repeat our analysis of the stationary solutions: Typically $E_0 = g(J)$ would now be different from a fixed point of the discrete mapping (2.4), so that the uniform field profile would not be a stationary solution of the discrete equations. The closest to the uniform solution would be a monotonic field profile where a fixed point of (2.4) is reached after a few iterations. For very long superlattices the difference from the results obtained with (1.6) is small. Nonuniform two-domain solutions would still be possible: after a few iterations E_j would be close to the first fixed point of the mapping and the rest of our analysis in Sec. II can be used to construct the nonuniform solutions. The differences would,

of course, be more noticeable for short superlattices. If (for example) $E_0 = g(J)$ turns out to be small [think, for instance, of a linear law $g(J) = rJ$ with a small resistivity r], there would be a region of the superlattice with a field smaller than that corresponding to the low-field domain of Sec. II. These differences should be experimentally testable, and in the absence of such tests and given the present good agreement with known facts,[1,4] we prefer to stick to the simpler situation provided by the boundary condition (1.6). Should future data force another choice of boundary condition upon us, our methodology could obviously be used to analyze the corresponding problem.

Our theory compares favorably with previous ones. Grahn et al.[4] considered a continuous Poisson equation that ignored the holes and a stationary Ampère's law with a drift velocity consisting of a sum of δ functions. They imposed a steplike stationary electric-field profile as a solution and obtained several qualitative features of the experimentally observed domains. Their results share with ours the fact that the average of the stationary current density at the branches representing nonuniform states is flat (independent of the applied bias, Sec. II). Dynamics and stability properties of nonuniform profiles were not considered in Ref. 4.

Laikhtman's theory[12] consists of a discrete Ampère's law plus the condition that the total voltage bias is constant. He did not consider the carrier densities and equations for them (Poisson's law and a rate equation for the holes). Thus the only coupling between quantum wells in his theory comes from the bias condition and the electric field in the wells may alternate between values at the different branches of $v(E)$ without restrictions. Then quite complicated nonmonotonic stable stationary field profiles with several domains are possible, as indicated in Ref. 12. Within Laikhtman's theory these profiles cannot be eliminated: the only possible correlation between domains would be caused by assuming coherent tunneling transport between wells. Our model yields monotonic nonuniform stationary profiles in a natural way without appealing to coherent tunneling. The number of possible nonuniform stationary states is also much smaller than in Ref. 12.

Korotkov et al.'s theory[13] corresponds to quite different superlattices (slim) where the tunneling processes are single-electron tunneling events and the charge is quantized. Interesting effects are predicted in this limit: coexistence of Bloch oscillations and oscillations due to single-electron tunneling.[24]

Other theories are based upon drift-diffusion models and are unable to reproduce important qualitative features present in the experiments, such as the multiplicity of steady states in the NDR region, and the eventual damping of the oscillations with time.[8] In fact, our model resembles known drift-diffusion models in the continuum limit (such as the one in Ref. 25), for which the uniqueness of the steady state can be proved easily, at least in the limit of small diffusion coefficient[26] [these continuum drift-diffusion models are also known to have Gunn effect oscillations[27,28] among their possible solutions,[29] which is not the case for Eqs. (1.12)–(1.16)]. Thus it seems that the discreteness of our model is a crucial ingredient

in reproducing both important static and dynamical features of transport in a superlattice made out of weakly coupled quantum wells. Work on derivation of discrete drift models from microscopic ones is now in progress.

ACKNOWLEDGMENTS

APPENDIX: LINEAR STABILITY OF THE STEADY SOLUTIONS

Linearization of Eqs. (1.12)–(1.16) about any steady solution (denoted by E_j^0, n_j^0, p_j^0, and J) yields the following system for the disturbances ($\hat{e}_j$, $\hat{n}_j$, $\hat{p}_j$, and $\hat{J}$) from it:

$$\hat{e}_j - \hat{e}_{j-1} = \hat{n}_j - \hat{p}_j, \tag{A1}$$

$$\beta \frac{d\hat{e}_j}{dt} = \hat{J} - v(E_j^0)\hat{n}_j - n_j^0 v'(E_j^0)\hat{e}_j, \tag{A2}$$

$$\frac{d\hat{p}_j}{dt} = -n_j^0 \hat{p}_j - p_j^0 \hat{n}_j, \tag{A3}$$

$$\sum_{j=1}^{N} \hat{e}_j = 0, \tag{A4}$$

$$\hat{e}_0 = \hat{e}_1, \tag{A5}$$

where, as usual, j runs from 1 to N. The system above can be reduced: we can eliminate the $\hat{n}$'s in favor of the $\hat{p}$'s and the $\hat{e}$'s by using (A1) and (A5). Moreover, summing (A2) for all $j = 1, \ldots, N$, and using (A4), we obtain $\hat{J}$ in terms of the same variables. Finally, a system of $2N$ equations (A2) and (A3) for the $2N$ unknowns ($\hat{e}_j$, $\hat{p}_j$, $j = 1, \ldots, N$) results. Time evolution preserves a constant value for the sum of all the fields, but the condition that this value be zero is to be imposed as an additional constraint to the resulting system of equations. They can be written in matrix form as $dx/dt = Mx$, where we have defined the vector $x = (\hat{e}_1, \ldots, \hat{e}_N, \hat{p}_1, \ldots, \hat{p}_N)^T$ (T denotes the transpose). The eigenvalues of M should in principle determine the linear stability of the steady solutions; in practice, however, one of the eigenvalues of M is spurious and we should eliminate it by taking into consideration the constraint (A4).

We can find the exact eigenvalues for the uniform solution (2.2) and (2.1). In this case, the matrix M is

$$M = \begin{pmatrix} A_{ee} & A_{ep} \\ A_{pe} & A_{pp} \end{pmatrix}, \tag{A6}$$

where

$$A_{ee} = -\frac{v}{\beta N}A - \frac{v}{\beta}B - \sqrt{\gamma}\frac{v'}{\beta}I + \frac{\sqrt{\gamma}\,v'}{\beta N}F, \tag{A7}$$

$$A_{ep} = \frac{v}{\beta N}F - \frac{v}{\beta}I, \tag{A8}$$

$$A_{pe} = -\sqrt{\gamma}B, \tag{A9}$$

$$A_{pp} = -2\sqrt{\gamma}I. \tag{A10}$$

Here v and v' denote $v(\phi)$ and $v'(\phi)$, respectively, I is the $N \times N$ identity matrix, and A, B, and F are the following $N \times N$ matrices:

$$A = \begin{pmatrix} 1 & 0 & \cdots & 0 & -1 \\ \vdots & \vdots & & \vdots & \vdots \\ \vdots & \vdots & & \vdots & \vdots \\ \vdots & \vdots & & \vdots & \vdots \\ 1 & 0 & \cdots & 0 & -1 \end{pmatrix}, \tag{A11}$$

$$B = \begin{pmatrix} 0 & \cdots & \cdots & \cdots & 0 \\ -1 & 1 & 0 & \cdots & 0 \\ 0 & -1 & 1 & \ddots & \vdots \\ \vdots & \ddots & \ddots & \ddots & 0 \\ 0 & \cdots & 0 & -1 & 1 \end{pmatrix}, \tag{A12}$$

$$F = \begin{pmatrix} 1 & \cdots & 1 \\ \vdots & & \vdots \\ 1 & \cdots & 1 \end{pmatrix}. \tag{A13}$$

The matrix M has only four distinct eigenvalues, given by the expressions

$$\lambda_0 = 0, \tag{A14}$$

$$\lambda_1 = -2\sqrt{\gamma}, \tag{A15}$$

$$\lambda_{\pm} = -\sqrt{\gamma}\left(1 + \frac{v'}{2\beta}\right) - \frac{v}{2\beta}$$

$$\pm\sqrt{\frac{v}{4\beta^2}(v + 2v'\sqrt{\gamma}) + \gamma\left(1 - \frac{v'}{2\beta}\right)^2}. \tag{A16}$$

The two first eigenvalues are simple: λ_0 is the spurious eigenvalue, corresponding to the eigenvector $(1,\ldots,1,0,\ldots,0)^T$ (notice that $\sum_{j=1}^{N}\hat{e}_j \neq 0$ for this eigenvector) and therefore it has to be ignored; λ_1 corresponds to the eigenvector $(0,\ldots,0,1,\ldots,1)^T$ and it is always real and negative. The remaining two eigenvalues (λ_+ and λ_-) have algebraic multiplicity $N-1$ each. It is not difficult to check that they are always real and that

at least one is always negative. Accordingly, the stability of the uniform solution depends on the sign of the other eigenvalue. It is simpler to consider the sign of the product $\lambda_+\lambda_-$. The solution will be unstable whenever this product is negative and neutrally stable when it is zero, i.e. when

$$v + 2\sqrt{\gamma}v' = 0.$$

This equation is exactly (2.8). Its minimum is γ_1, the photoexcitation below which the uniform solution is the only existing stationary state.

It is clear that we could in principle ascertain the linear stability of any steady solution of (1.12)–(1.16) by the method so far explained. We would use any of the well known diagonalization numerical routines on the matrix M corresponding to the steady solution. However, these routines quite disastrously fail to determine the exact value of the eigenvalue of M because of the high multiplicity thereof: the errors of the numerically determined eigenvalues can be as high as 10%, and, what is even worse, they become artificially simple and sometimes even acquire a spurious imaginary part. The fact that the matrix M for the uniform steady solution is not diagonalizable increases the numerical difficulty. It is important to notice that the linear stability of the uniform stationary solution is not affected by these numerical errors: it depends only on the *sign* of the largest eigenvalue and we have checked that this sign is given correctly by the numerical code [we have always compared the results provided by the code with the formula (A16) with the $+$ sign that yields the largest eigenvalue exactly].

It could seem that these numerical troubles due to eigenvalue degeneracy may not appear for domain-type steady solutions (which are nonuniform). However, we do not now have *exact* means of checking this conjecture at our disposal. Thus our numerical determination of the linear stability of domain-type steady solutions has always been confronted with the results of direct simulation of the full system of equations whenever the comparison was possible. We have found that (as in the case of the uniform solution) the linear stability of the nonuniform steady states is correctly predicted by the numerical determination of the eigenvalues. There is a reasonable agreement between the two numerical procedures for the real part of the largest eigenvalue while there are large errors for the imaginary part. Thus while the eigenvalue calculation gives acceptable estimations of the *damping* of the photocurrent oscillations, it provides poor estimations of the *frequency*. Hence the stability properties of a given stationary state are well determined by the numerical procedure and we have used it, together with the simulations, to delimit the region of the γ-ϕ phase diagram (Fig. 5) inside which stable nonuniform stationary solutions exist. Work on devising reliable numerical codes to determine the oscillation frequency from the eigenvalues is now in progress.

* Present address: Department of Physics, Ohio State University, 174 W. 18th Ave., Columbus, OH 43210-1106.

[1] S.-H. Kwok, Ph.D. thesis, University of Michigan, Ann Arbor, 1994. See also S.-H. Kwok, R. Merlin, L. L. Bonilla, J. Galán, J. A. Cuesta, F. C. Martínez, J. M. Molera, H. T. Grahn, and K. Ploog (unpublished).

[2] R. E. Cavicchi, D. V. Lang, D. Gerhoni, A. E. Sergent, H. Temkin, and M. B. Panish, Phys. Rev. B **38**, 13 474 (1988).

[3] H. T. Grahn, H. Schneider, and K. von Klitzing, Appl. Phys. Lett. **54**, 1757 (1989).

[4] H. T. Grahn, H. Schneider, and K. von Klitzing, Phys. Rev. B **41**, 2890 (1990).

[5] S.-H. Kwok, E. Liarokapis, R. Merlin, and K. Ploog, in *Light Scattering in Semiconductor Structures and Superlattices*, edited by D. J. Lockwood and J. F. Young (Plenum Press, New York, 1991), p. 491.

[6] H. T. Grahn, W. Müller, K. von Klitzing, and K. Ploog, Surf. Sci. **267**, 579 (1992).

[7] L. Esaki and L. L. Chang, Phys. Rev. Lett. **33**, 495 (1974).

[8] H. Le Person, C. Minot, L. Boni, J. F. Palmier, and F. Mollot, Appl. Phys. Lett. **60**, 2397 (1992).

[9] R. F. Kazarinov and R. A. Suris, Fiz. Tekh. Poluprovodn. **6**, 148 (1972) [Sov. Phys. Semicond. **6**, 120 (1972)].

[10] F. Capasso, K. Mohamed, and A. Y. Cho, Appl. Phys. Lett. **48**, 478 (1986).

[11] H. T. Grahn, H. Schneider, W. W. Rühle, K. von Klitzing, and K. Ploog, Phys. Rev. Lett. **64**, 2426 (1990).

[12] B. Laikhtman, Phys. Rev. B **44**, 11 260 (1991).

[13] A. N. Korotkov, D. V. Averin, and K. K. Likharev, Appl. Phys. Lett. **62**, 3282 (1993).

[14] J. Shah, *Hot Carriers in Semiconductor Nanostructures: Physics and Applications* (Academic Press, Boston 1992), p. 279.

[15] F. Capasso, K. Mohamed, A. Y. Cho, R. Hull, and A. L. Hutchinson, Phys. Rev. Lett. **55**, 1152 (1985).

[16] K. Seeger, *Semiconductor Physics: An Introduction*, 4th ed. (Springer, New York 1989).

[17] *Heterojunctions and Semiconductor Superlattices*, edited by G. Allan, G. Bastard, N. Boccara, M. Lannoo, and M. Voos (Springer, Berlin, 1986).

[18] H.-J. Polland, L. Schultheis, J. Kuhl, E. O. Göbel, and C.

W. Tu, Phys. Rev. Lett. **55**, 2610 (1985).

[19] At this point all the $N - 1$ nonuniform solution branches (with $2 \rightarrow 3$ jumps) coalesce with the uniform solution, which has a zero eigenvalue of multiplicity $N-1$. For a given $\gamma > \gamma_1$, the difference between the biases corresponding to two contiguous branches of these nonuniform solutions in Fig. 3 (with the same J) is equal to $(E_N - E_L)/N$, where the E_j correspond to the solution branch with larger bias, with $E_j = E_L$ for $1 \leq j \leq k$. Let now $0 < (J - J_2) \ll 1$. Then it is straightforward to check that the difference between the biases of contiguous nonuniform solution branches is $O[(J - J_2)^{2^{-(N-k-1)}}/N]$. Clearly this difference shrinks to zero at $J = J_2$ for any fixed N.

[20] Notice that, while we have chosen the shape of $v(E)$ to reproduce this fact, the uniqueness and stability of this solution at low laser power are a result of our theory.

[21] D. A. B. Miller, D. S. Chemla, T. C. Damen, A. C. Gossard, W. Wiegmann, T. H. Wood, and C. A. Burrus, Phys. Rev. Lett. **53**, 2173 (1984).

[22] R. Merlin (private communication).

[23] For doped superlattices we do not need the photoexcitation to generate carriers. We have found that the corresponding discrete equations have persistent time-dependent oscillations of the current, confirming the damping role of the processes involving the holes.

[24] A. N. Korotkov, D. V. Averin, and K. K. Likharev, Phys. Rev. B **49**, 1915 (1994).

[25] S. W. Teitsworth, Appl. Phys. A **48**, 127 (1989); L. L. Bonilla and S. W. Teitsworth, Physica D **50**, 545 (1991).

[26] L. L. Bonilla, Phys. Rev. B **45**, 11 642 (1992).

[27] M. P. Shaw, H. L. Grubin, and P. R. Solomon, *The Gunn-Hilsum Effect* (Academic, New York, 1979); M. P. Shaw, V. V. Mitin, E. Schöll, and H. L. Grubin, *The Physics of Instabilities in Solid State Electron Devices* (Plenum, New York, 1992).

[28] F. J. Higuera and L. L. Bonilla, Physica D **57**, 161 (1992).

[29] I. R. Cantalapiedra, L. L. Bonilla, M. J. Bergmann, and S. W. Teitsworth, Phys. Rev. B **48**, 12 278 (1993); L. L. Bonilla, I. R. Cantalapiedra, M. J. Bergmann, and S. W. Teitsworth, Semicond. Sci. Technol. **9**, 599 (1994).
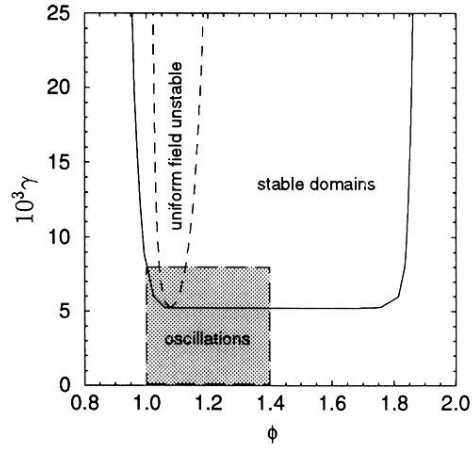
FIG. 5. Phase diagram of the model: laser power (γ) vs voltage bias (ϕ). Stable nonuniform solutions with domains exist only inside the continuous curve. Inside the dashed line the uniform solution is unstable. The shaded rectangle approximately delimits the region where oscillations of the PC (i.e., of the domain wall of the electric-field profile) can be obtained.
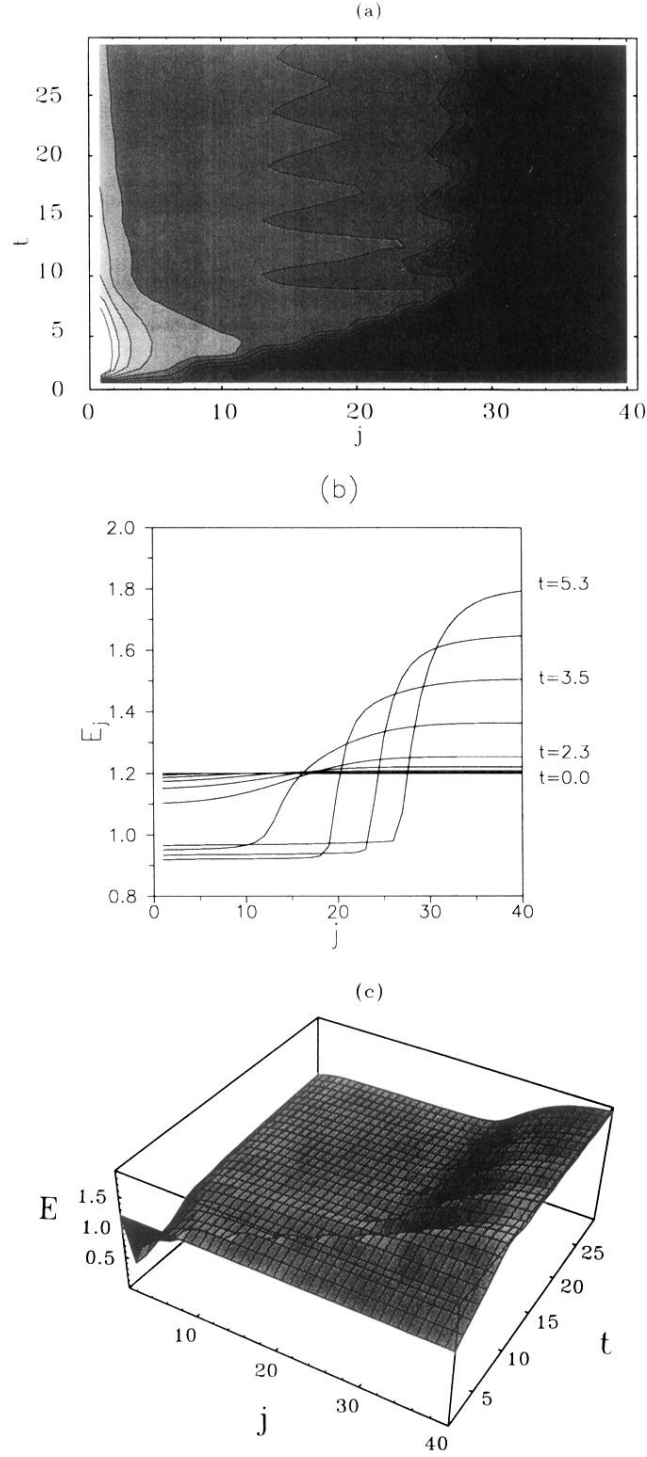
(a)

(b)

(c)

FIG. 6. Evolution of the domain wall in time for $\gamma = 2 \times 10^{-3}$ and $\phi = 1.2$. (a) is a contour plot with time flowing on the y axis and the quantum well number on the x axis. The electric-field contours go from 0.5 to 1.7 in 0.1 steps. At $t = 0$ we start with the uniform solution. The perturbation is clearly visible at the first well at short times. The creation and the displacement of the domain wall can be visualized. At $t = 0.5$ the two domains are already defined (the darker the figure the higher the electric field) and the domain wall begins to oscillate. Most of the wells have an electric field centered around the first maximum of $v(E)$ (low-field domain). In (b) we represent the electric-field profile at short times (domain formation) and in (c) the domain wall oscillations.